Spatio-temporal TGV denoising for ASL perfusion imaging

Stefan M. Spann[a], Kamil S. Kazimierski[c], Christoph S. Aigner[a,b], Markus Kraiger[a], Kristian Bredies[c], Rudolf Stollberger[a,b,*]

[a] Institute of Medical Engineering, Graz University of Technology, Stremayrgasse 16, 8010 Graz, Austria
[b] BioTechMed-Graz, Graz, Austria
[c] Institute for Mathematics and Scientific Computing, University of Graz, NAWI Graz, Heinrichstrasse 36, 8010 Graz, Austria

ARTICLE INFO

ABSTRACT

In arterial spin labeling (ASL) a perfusion weighted image is achieved by subtracting a label image from a control image. This perfusion weighted image has an intrinsically low signal to noise ratio and numerous measurements are required to achieve reliable image quality, especially at higher spatial resolutions. To overcome this limitation various denoising approaches have been published using the perfusion weighted image as input for denoising. In this study we propose a new spatio-temporal filtering approach based on total generalized variation (TGV) regularization which exploits the inherent information of control and label pairs simultaneously. In this way, the temporal and spatial similarities of all images are used to jointly denoise the control and label images. To assess the effect of denoising, virtual ground truth data were produced at different SNR levels. Furthermore, high-resolution in-vivo pulsed ASL data sets were acquired and processed. The results show improved image quality, quantitative accuracy and robustness against outliers compared to seven state of the art denoising approaches.

Introduction

Arterial spin labeling (ASL) (Detre et al., 1992) is a powerful magnetic resonance imaging (MRI) approach to measure cerebral blood flow (CBF). ASL is completely non-invasive and uses magnetically labeled blood water as an endogenous tracer. Therefore, it is highly suitable for repetitive follow-ups and allows for absolute quantification of CBF. In addition, ASL is eligible for functional activity and connectivity studies, with important advantages compared to blood oxygenation level dependent (BOLD) -MRI: a direct activation related CBF change (Detre et al., 1992), a higher spatial accuracy and a higher intra-individual reproducibility (Raoult et al., 2011). These benefits make this method highly interesting in both clinical and research areas (Zhang, 2016). Recommendations for clinical robust ASL perfusion MRI were recently published by the ISMRM Perfusion Study Group and the European Consortium for ASL in Dementia (Alsop et al., 2015).

However, all these benefits are challenged by a low signal to noise ratio (SNR) with a typical signal change between control and label image of about 1.5% (Petr et al., 2010a). Thus, typically 20–50 image-pairs with low in-plane resolutions (3–4 mm) and through plane resolutions (4–8 mm) are acquired to achieve sufficient SNR (Alsop et al., 2015; Bammer, 2016). This coarse spatial resolution is prone to partial volume effects (PVE) in the CBF images leading to significant

CBF quantification errors in the gray and white matter (Liang et al., 2013; van Gelderen et al., 2008). This is problematic for applications in different diseases and in case of group studies especially in age-related (Asllani et al., 2009; Fazlollahi et al., 2015) and activation studies (Borogovac et al., 2010).

To reduce the influence of partial volume effects several methods were proposed based on high resolution T1 images (Asllani et al., 2008; Liang et al., 2013; Petr et al., 2010a). Prerequisites of these methods are accurate segmentation as well as subsequent registration with the ASL image. However, these two steps are often prone for errors and the effect of PVE correction comes at the cost of a bias and spatial smoothing (Fazlollahi et al., 2015). Another, more direct way to avoid partial volume effects, is to increase the resolution in the ASL images. A smaller voxel size is also beneficial for the location of small hypo- and hyper perfusion lesions (Liang et al., 2013). A higher resolution comes with the hurdle of a reduced SNR which can be compensated by increasing the number of averages. Compensation by increasing the number of averages can lead to impractical long scanning time and additional sensitivity for motion artifacts.

Improvements were achieved through advanced implementations of ASL methods such as pseudo-continuous labeling (PCASL) (Dai et al., 2008) or 3D imaging techniques (Günther et al., 2005; Vidorreta et al., 2013). In addition, the continued advancements of MR imager

---

hardware provide one solution to the limited signal yield. Several studies indicated the potential of higher field strength for ASL MRI due to the higher SNR and prolonged T1 of blood and tissue (Bause et al., 2016; Gardener et al., 2009; Pfeuffer et al., 2002; Teeuwisse et al., 2010; Wang et al., 2002). However, ASL at stronger fields presents several challenges: stronger susceptibility artifacts, higher SAR and compromised labeling efficiency due to inhomogeneities in B1 and B0 fields (Teeuwisse et al., 2010).

Data post-processing methods such as motion correction (Wang, 2012; Wang et al., 2008), temporal filtering and outlier correction (Behzadi et al., 2007; Fang et al., 2015; Maumet et al., 2014; Shirzadi et al., 2015; Tan et al., 2009; Wang, 2012) provide increased SNR, improved perfusion quantification and image quality and increased reproducibility (Fazlollahi et al., 2015) by eliminating corruptions in the acquired data. Further improvements are achieved using standard denoising for the images. Several groups have studied the performance of denoising techniques applied to ASL images. Different denoising strategies were proposed, for example denoising in the wavelet domain (Bibic et al., 2010; Wells et al., 2010), in the image domain using adaptive filtering (Wells et al., 2010), non-local means filtering (Petr et al., 2010b), combination of non-local means filtering with wavelet domain filtering (Liang et al., 2015) or total variation denoising in combination with tissue partial volume effect correction (Petr et al., 2010a). All denoising methods use the perfusion weighted image (control − label) as input for denoising to improve the robustness of the CBF quantification (Fazlollahi et al., 2015).

In the present work, we propose a total generalized variation (TGV) (Bredies et al., 2010) based denoising approach that is matched to the label control image pair time series of ASL MRI. The TGV has already been successfully applied to medical image reconstruction and denoising in MRI (Knoll et al., 2011). The proposed TGV-based denoising approach combines temporal and spatial information for improving the image quality of ASL images. The incorporation of temporal information in the denoising process may be additionally beneficial for detecting outliers.

The purpose of this study is to evaluate the performance of this novel technique and its influence on the CBF quantification in comparison to recently published and well established denoising techniques. The evaluation is done on synthetic and experimental in-vivo high and standard resolution pulsed ASL (PASL) data with varying numbers of control-label pairs.

Materials and methods

Subjects

Eight healthy volunteers (25.5 ± 1.2 years old with a range of 24–28, 4 women) were included in this study after giving a written informed consent. Caffeine and tobacco ingestion were avoided before the MR acquisition to preclude alterations on the global and regional CBF (Addicott et al., 2009; Domino et al., 2004; Vidyasagar et al., 2013).

MRI-Acquisition

The ASL experiments were carried out on a 3 T MR system (Magnetom Skyra, Siemens Healthcare, Germany). Pulsed ASL measurements were performed on eight healthy subjects using PICORE (Wong et al., 1997) – Q2TIPS (Luh et al., 1999) with a 32-channel head coil. Small wedge sponges were placed between the patient's head and the coil to reduce motion during the acquisition.

The following acquisition parameters were used: 12 slices, 3.6 mm thickness, distance factor 25%, matrix 128×128, field-of-view (FOV) 230×230 mm^2, in-plane resolution 1.8×1.8 mm^2, 6/8 partial Fourier, GRAPPA-factor 2 and pre-scan normalization. Imaging was conducted with single-shot echo planar imaging (EPI) with TR/TE = 2800/19 ms,

flip angle = 90°, bolus duration TI_1 = 800 ms, labeling inversion time TI_2 = 1800 ms, labeling slab thickness 100 mm, 2 cm gap between labeling slab and image slice, ascending slice order and bandwidth = 1630 Hz/px. To compute an unfiltered reference perfusion weighted image, 500 control/label-pairs (C/L-pairs) and one proton density weighted (M_0) image were acquired within a total scanning time of 45 min.

Additionally, anatomical T1 weighted images were acquired for each subject using a 3D magnetized prepared rapid gradient echo (MPRAGE) sequence with $1 \times 1 \times 1$ mm^3 resolution, field of view = 256 $\times$ 256 mm^2, 144 slices, TR/TE/TI = 1910/1.81/1000 ms, and flip angle = 8°.

In addition, we acquired standard resolution ASL images from 2 subjects with the following parameters: 12 slices, 6 mm thickness, distance factor 25%, matrix 64×64, field-of-view (FOV) 192 $\times$ 192 mm^2, in-plane resolution 3×3 mm^2, 6/8 partial Fourier, bandwidth = 1630 Hz/px and pre-scan normalization. All other imaging parameters were the same as for the high resolution ASL dataset. To compute an unfiltered reference perfusion weighted image, 100 control/label-pairs (C/L-pairs) and one proton density weighted (M_0) image were acquired within a total scanning time of 9 min 25 s.

Anatomical image processing

For each subject, the acquired T1 weighted image was segmented into white-matter (WM), gray-matter (GM) and cerebrospinal fluid (CSF) regions using Statistical Parameter Mapping v.12 (SPM12, Wellcome Trust Centre for Neuroimaging, London, UK; www.fil.ion. ucl.ac.uk/spm). The results of the segmentation process were tissue partial volume content (PV-content) maps defining the amount or content of GM, WM and CSF in each voxel. These tissue PV-content maps and the T1 weighted images were coregistered to the ASL space using the first ASL-image as a reference. Afterwards the resulting coregistered tissue PV-content maps were used to create a brain mask. The CSF, WM and GM PV-content maps were summarized resulting in a single PV-content map. In this map all voxels with a tissue PV-content greater than 0.1 were included in the brain mask, which delivers good results.

High resolution synthetic dataset

High resolution synthetic image sets were generated from one subject (subject 8) based on the acquired M_0 image and the coregistered WM and GM PV-content maps (Bibic et al., 2010). In order to create a noise free CBF-map, CBF values of 20 ml/100 g/min and 65 ml/100 g/min (Leenders et al., 1990; Zhang et al., 2014), reported for the normal human brain, were assigned to the WM (f_{WM}) and GM (f_{GM}) voxel respectively. To incorporate realistic partial volume effects in the synthetic images, the GM and WM PV-content maps were multiplied using the following equation:

$$f(x, y, z) = f_{GM} P_{GM}(x, y, z) + f_{WM} P_{WM}(x, y, z), \quad (1)$$

where $P_{GM}(x,y,z)$ is the PV-content map of GM defining the content of GM in the voxel at location (x,y,z), $P_{WM}(x,y,z)$ is the PV-content map of WM defining the content of WM in the voxel at location (x,y,z).

The control image C was assumed to be the M_0 image and the label image L was calculated in each voxel by using a general kinetic model (Buxton et al., 1998)

$$L(x, y, z) = C(x, y, z)$$
$$- \frac{2 \cdot \alpha \cdot M_0(x, y, z) \cdot f(x, y, z) \cdot TI_1 \cdot e^{-\frac{TI_2}{T1_b}}}{\lambda}, \quad (2)$$

where α is the labeling efficiency and set to 0.98 (Wong et al., 1998), TI_1 is the labeling duration and set to 800 ms, TI_2 is the labeling inversion time and set to 1800 ms (Alsop et al., 2015). M_0 is the
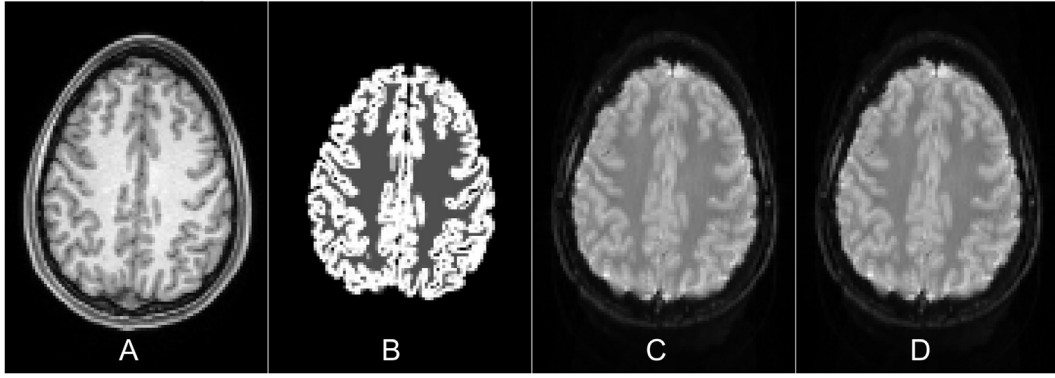
Fig. 1. Coregistered and resampled T1 weighted image in the ASL space (A) with voxel dimensions of $1.8 \times 1.8 \times 3.6$ mm^3 of subject 8. Synthetic, noise free CBF-map (B) created from the coregistered white and gray matter PV-content maps. Noise free synthetic control (C) and label image (D).

acquired proton density image, λ is the blood-brain partition coefficient and set to 0.9 ml/g (Herscovitch and Raichle, 1985), T1$_b$ is the longitudinal relaxation time of blood at 3 T and set to 1650 ms (Lu et al., 2004) and f(x,y,z) is the synthetic CBF-map generated as described in Eq. (1).

The computed synthetic CBF-Map, the Control and Label image are illustrated in Fig. 1.

To compute a synthetic dataset with a realistic noise level, the standard deviation over the 500 repetitions was estimated from the acquired high-resolution C and L images for each voxel. Subsequent Gaussian noise with a standard deviation previously estimated was added to each voxel of the synthetic noise free C and L images. This step was repeated 500 times to generate a synthetic data pool containing 500 C/L-pairs.

The benchmark for the synthetic datasets consisted of 50 trials with 40, 50, 60, 80 and 100 randomly selected image pairs out of a data pool of 500.

ASL data preprocessing

ASL image preprocessing was performed on the high and standard resolution in-vivo datasets using SPM12, MATLAB 2015b (The MathWorks, Inc., Natick, Massachusetts, USA), ASL-toolbox (Wang, 2012; Wang et al., 2008) and in-house MATLAB scripts. Prior to spatial denoising, ASL datasets were preprocessed using the steps and algorithm recommended by Fazlollahi et al. (2015). First, the acquired ASL images were motion corrected using the ASL-toolbox. This involves realigning of all ASL images, including all label and control images, to the first ASL image (L) in the time series for estimating the rigid motion time course. Subsequently, errors in realignment resulting from the control/label intensity difference were regressed out from the motion time course as described in Wang (2012) and finally the clean motion parameters were used for motion-correction. In a second step the whole ASL time series was de-trended to remove baseline drifts. Therefore, a first order high-pass Butterworth filter with a cutoff frequency of 0.01 Hz was applied to the ASL-image time series (L/C/L/C...) as described in Wang (2012) and Wang et al. (2013). Third, residual motion artifacts and global signal fluctuations were regressed out of the ASL image time series at each voxel (Wang, 2012). Prior to spatial denoising outlier C/L-pairs were removed using Z-score thresholding (Tan et al., 2009).

In-vivo dataset

The motion corrected, de-trended and outlier removed C/L-pairs served as a basis for all subsequently applied denoising methods.

For the high resolution in-vivo dataset of subject 8, which was used to create the synthetic dataset, benchmarking was performed similar to the synthetic dataset and consisted of 50 trials with 40, 50, 60, 80 and

100 randomly selected image pairs out of a data pool of 500. For the evaluation of the remaining 7 high resolution in-vivo datasets, 50 trials with 50 randomly selected image pairs out of the acquired 500 were used.

For the two standard resolution datasets, benchmarking was performed using 50 trials with 5, 8, 10, 12, 15, 20 and 25 randomly selected image pairs out of a data pool of 100.

Denoising of ASL datasets

TGV – image model

Images encountered in medical imaging can be modeled as smooth areas divided by jumps or cliffs. This is the typical image model in medical imaging. This idea is mathematically formalized by defining a function, which produces low values for images belonging to the model, and producing high values for images not belonging to the model. This function is then called the functional of the image model.

One well-known formalization of the above image model is total variation (functional) (TV) (Rudin et al., 1992). However, the main and crucial disadvantage of TV is that it tends to produce the so-called stair-stepping artifacts (Dobson and Santosa, 1996). In order to alleviate this disadvantage, the total generalized variation functional (TGV) was introduced in Bredies et al. (2010). For an analytic derivation of TGV we refer to Bredies et al. (2010). In the following we employ the formulation presented in Bredies and Valkonen (2011). In the discretized form the TGV functional is given by

$$\mathrm{TGV}(\alpha_1, \alpha_0; u) = \min_v \{\alpha_1 \cdot \|\nabla u - v\|_1 + \alpha_0 \cdot \|\mathcal{E}v\|_1 \}. \tag{3}$$

In the above formula α_1 and α_0 are parameters controlling the strength of image model assumptions and u is an image. Further, ∇ and $\mathcal{E}$ are appropriate discretizations of the gradient respectively of the symmetrized derivative $\mathcal{E}v = \frac{1}{2}(\nabla v + (\nabla v)^T)$. For details of the discretization of the involved operators and norms confer (Bredies, 2014). The TGV norm decomposes the gradient in a smooth part v and a gradient remainder $\nabla u - v$, which allows for smooth structures between jumps in the function u itself. For $\alpha_0 >> \alpha_1$ the functional will tend to behave like a TV functional, on the other hand for $\alpha_1 >> \alpha_0$ only the non-smooth parts of the gradient are penalized which results in penalty known as TV^2. For a systematic study of related functionals consider (Pöschl and Scherzer, 2015).

Denoising setup

Mathematically the aim is to recover an estimate of the control data u_c and label data u_l from the given measured control data u_c^d and label data u_l^d. One notices that u_c^d is a stack of images, each of the size of u_c. The same holds for u_l^d and u_l. In order for u_c, when stacked, to be a robust estimate of u_c^d it should minimize $\|Su_c - u_c^d\|_1$. The minimization of the previous norm on its own leads to the elementwise median of u_c^d

with respect to the stack (temporal) dimension. The operator $\mathcal{S}$ is assumed to replicate as many images of size of u_c as are needed in order to get a stack of the same size as u_c^d. For similar reasons u_l should minimize $\|\mathcal{S}u_l - u_l^d\|_1$. Next, u_l should adhere to the image model proposed above. Therefore, it should minimize TGV$(\alpha_1, \alpha_0; u_l)$. In a last step one is tempted to propose that u_c should also adhere to the image model by minimizing a related TGV functional. However, one observes that, the images u_c and u_l have a much higher dynamical range than the difference of the denoised images. Further, the difference of these images is the key quantity in ASL applications. Therefore, far superior results are to be expected if one forces the difference to adhere to the image model by minimizing TGV$(\alpha_1, \alpha_0; u_c - u_l)$. Altogether u_c and u_l should be chosen such that the functional

$$\|\mathcal{S}u_c - u_c^d\|_1 + \|\mathcal{S}u_l - u_l^d\|_1 + \text{TGV}(\alpha_1, \alpha_0; u_l) + \text{TGV}(\alpha_1, \alpha_0; u_c - u_l), \tag{4}$$

is minimal. Notice, that by similar argumentation the term TGV$(\alpha_1, \alpha_0; u_l)$ could also be replaced by TGV$(\alpha_1, \alpha_0; u_c)$. In our experience the differences between both cases are negligible. In order to control the weighting between the two TGV functional an additional parameter $s \in [0,1]$ is introduced

$$\|\mathcal{S}u_c - u_c^d\|_1 + \|\mathcal{S}u_l - u_l^d\|_1 + \gamma_1(s)\text{TGV}(\alpha_1, \alpha_0; u_l)$$
$$+ \gamma_2(s)\text{TGV}(\alpha_1, \alpha_0; u_c - u_l). \tag{5}$$

The weights are chosen as described in Schloegl et al. (2016) to ensure that the overall costs of the functional does not reduce to zero:

$$\gamma_1(s) = \frac{s}{\min(s, 1-s)}, \gamma_2(s) = \frac{1-s}{\min(s, 1-s)}. \tag{6}$$

Furthermore, a regularization parameter λ was introduced, allowing the weighting between data fidelity versus regularization. This parameter is chosen according to the noise level of the datasets. Since the expected noise level in control and label image is nearly the same, the same regularization parameter is used for both data terms leading finally to the following functional:

$$\lambda\|\mathcal{S}u_c - u_c^d\|_1 + \lambda\|\mathcal{S}u_l - u_l^d\|_1 + \gamma_1(s)\text{TGV}(\alpha_1, \alpha_0; u_l)$$
$$+ \gamma_2(s)\text{TGV}(\alpha_1, \alpha_0; u_c - u_l). \tag{7}$$

Formulation as saddle-point problem

Any optimization method for non-smooth convex problems can be employed to solve the minimization problem presented in the last section. Due to the intrinsic structure of the problem, the algorithm of Chambolle and Pock (2011) was employed in the experiments. This algorithm ensures convergence to the global optimum. To that end the problem is reformulated as a saddle point problem (for details see Appendix):

$$\min_x \max_y \langle \mathcal{K}x|y\rangle + \mathcal{F}(x) - \mathcal{G}(y). \tag{8}$$

Parameter choice

Previous studies (Bredies and Holler, 2015; Knoll et al., 2011; Schloegl et al., 2016) have shown, that setting the ratio α_1/α_0 to $1/\sqrt{2}$ yields robust results and this ratio is used throughout this work. The model parameter s, which controls the weighting between the first TGV and the second TGV functional, was fixed for the high-resolution and low resolution in-vivo and synthetic dataset by evaluating a range of parameters with respect to the structural similarity index (SSIM) (Wang et al., 2004). The regularization parameter λ was optimized using a fixed s for different numbers of control/label pairs. For the training of the two parameters slice 6 of subject 8 was used for the high-resolution in-vivo dataset and slice 6 was used for the synthetic dataset. Exemplary results of the parameter tuning are shown in Fig. 2 for the in-vivo dataset. The used model and regularization parameters

for the high resolution datasets are summarized in Table 1. For the standard resolution ASL datasets we used the following parameters: $\alpha_1/\alpha_0 = 1/\sqrt{2}$, s = 0.575 and $\lambda = 6/\sigma$. For all experiments the number of iterations was set to 1000.

Reference denoising methods

We chose state of the art denoising methods which were successfully applied to ASL perfusion images in the past: Wavelet-based-Wiener (WbW) (Bibic et al., 2010), iterative-soft thresholding (Daubechies et al., 2004), adaptive Wiener (aWNR) (Wells et al., 2010), Anisotropic Diffusion (AD) (Wells et al., 2010), DT-CWT ONLM (Liang et al., 2015), spatio-temporal low rank total variation (STLRTV) (Fang et al., 2015) and additional block matching 3D (BM3D) (Dabov et al., 2007). Each of the denoising filters is parameter dependent and the choice of the right parameter has a major impact on the denoising result. For the choice of the parameters we decided to maximize the structural similarity index (SSIM) between the gold standard and denoised image to evaluate the performance of each filter in a fair way, rather than using an empiric optimization by visual inspection. Compared to the RMSE, the SSIM includes both the structure and the contrast of the image and therefore reflects the visual interpretation of the human eye in a better way (Wang et al., 2004). Some of the filters have noise-dependent parameters, for which the noise was estimated for each voxel over the number of repetitions. The mean standard deviation σ over all pixels within the brain mask was computed and used as standard deviation (Petr et al., 2010b).

Temporal mean filter

A perfusion weighted time series was calculated from the motion corrected, detrended and outlier cleaned control/label series by pairwise subtraction of the control/label-pairs. The single perfusion weighted images are so noisy, that the benefit of applying one of the highly sophisticated reference filters on these single images is very low. Furthermore, due to the subtraction of control and label images a separate denoising of these images leads to flatter edges compared to denoising the perfusion weighted image themselves (Wells et al., 2010). Therefore, a mean perfusion weighted image was generated by averaging the perfusion weighted time series. This mean perfusion weighted image serves as basis for all following reference denoising methods with the exception of the STLRTV-filter which uses the perfusion weighted time series as input for denoising.

Anisotropic diffusion (AD) filter

The AD filter method was implemented in MATLAB (Wells et al., 2010). For optimal performance of the filter the diffusion step time was set to 0.25 and the conduction coefficient K and the number of iterations were optimized as described above. Exemplary results of the parameter optimization process are shown in Fig. 3.

Adaptive Wiener (aWNR) filter

An adaptive Wiener filter based on the mean and variance in the local neighborhood of each voxel was implemented in MATLAB (Wells et al., 2010). The kernel size and the global noise variance were optimized to ensure that the filter delivers best possible results.

Iterative soft thresholding (Wav(S))

The iterative soft thresholding algorithm (Daubechies et al., 2004) was implemented in MATLAB for the LeGall 5/3 wavelet (Le Gall and Tabatabai, 1988). The number of iterations was set to 5000 and the threshold factor was optimized.

Wavelet based Wiener (WbW) filter

The WbW filter (Bibic et al., 2010) was implemented in MATLAB using the Wavelet Toolbox. For the best possible performance the threshold factor was optimized.
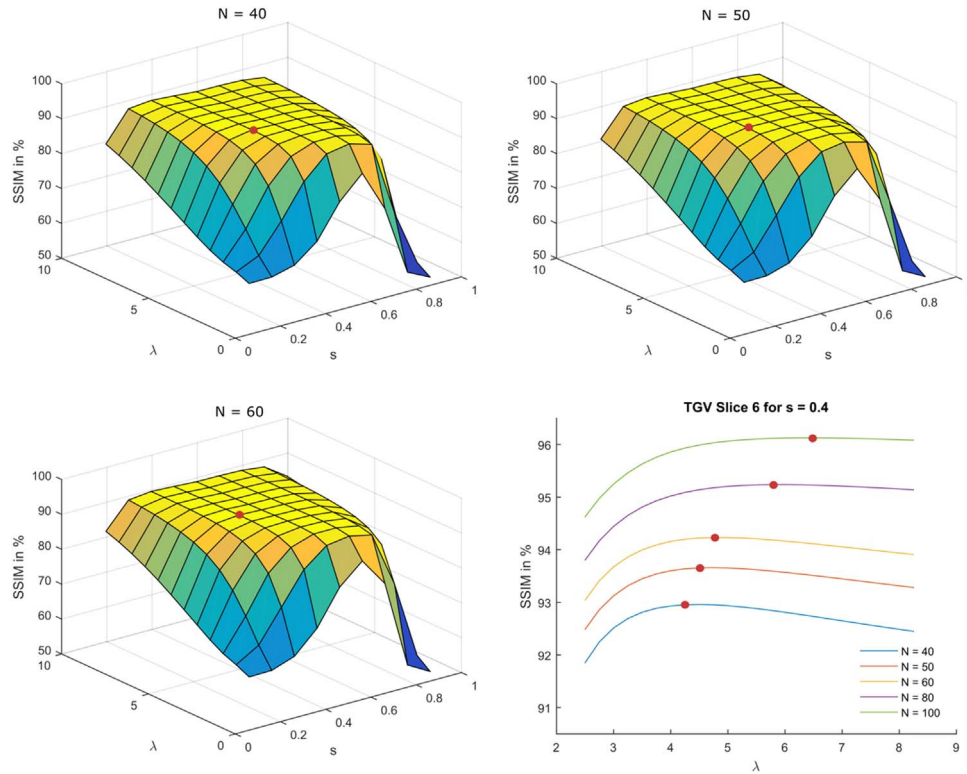
Fig. 2. Results of the parameter learning for the TGV-approach on high resolution in-vivo images using 40, 50 and 60 C/L-pairs for slice 6 of subject 8. The red point indicates the maximum SSIM-value. The maximum value is achieved setting the parameter s to 0.4. The parameter λ depends on the noise level.

Table 1

Choice of the model and regularization parameter for synthetic and high resolution in-vivo datasets.

Symbol	Number of C/L − pairs	Chosen value	
		Synthetic	In-vivo
Model parameter			
α_1/α_0	40,50,60,80,100	$1/\sqrt{2}$	$1/\sqrt{2}$
$s \rightarrow \gamma_{1,2}(s)$	40,50,60,80,100	0.475	0.4
Regularization parameter			
λ	40	2.15	4.25
	50	2.25	4.50
	60	2.45	4.75
	80	2.75	5.75
	100	3.00	6.50

Block matching 3D (BM3D) filter

The MATLAB implementation of the BM3D filter (Dabov et al., 2007) was used for denoising (http://www.cs.tut.fi/~foi/3D-DFT). The filter profile was set to "high" and the noise standard deviaws typical high resolutiotion σ was estimated as described above and scaled by a factor c to ensure best possible results in case that the noise level was not estimated sufficiently well.

Non-local means combined dual-tree complex wavelet transform (DT-CWT ONLM) filter

The MATLAB version of the DT-CWT ONLM filter (Liang et al., 2015) was used (https://www.nitrc.org/projects/dt-cwt-nlm). All 6 parameters (M1, M2, α_1, α_2, β_1 and β_2) were optimized to ensure the best possible performance.

Spatio-temporal low rank total variation (STLRTV) filter

The STLRTV filter was implemented in MATLAB as described in Fang et al. (2015). For the best possible performance of the filter the parameters λ_{TV} and λ_{rank} were optimized.

Quantification of CBF

For the quantification of the CBF a general kinetic model was applied (Buxton et al., 1998). According to this model, the cerebral blood flow in ml/100 g/min can be calculated in each voxel using the following equation:

$$f(x, y, z) = \frac{\lambda \cdot \Delta M(x, y, z)}{2 \cdot \alpha \cdot M_0(x, y, z) \cdot TI_1 \cdot e^{-\frac{TI_2}{T1b}}},$$

(9)

where ΔM is the denoised difference image and M_0 is the acquired proton density image smoothed with a Gaussian filter (FWHM = 3 mm) as recommended (Alsop et al., 2015). The total delay time TI_2 was set to 1800 ms for the leading slice. Because of using an EPI readout and acquiring the slices in ascending order, an extra delay of 80 ms was added to TI_2 for each further slice acquired in ascending order (Alsop et al., 2015). All other parameters were set to the same values as described in *Synthetic dataset*.

Evaluation

Two common metrics were used as a measure of denoising quality, the structural similarity index (SSIM) (Wang et al., 2004) and the peak signal to noise ratio (PSNR) (Fang et al., 2015; Liang et al., 2015). In case of the synthetic dataset the noise free CBF-map served as gold standard. For the experimental dataset the gold standard CBF-map was computed from the 500 C/L-pairs for the high resolution dataset and from the 100 C/L-pairs for the standard resolution dataset. All evaluation steps were performed on both, synthetic and experimental dataset.

SSIM

Image structure degeneration and contrast difference between the gold standard CBF-map and the denoised CBF-map were analyzed using the quantitative structural similarity index (SSIM) (Wang et al., 2004).
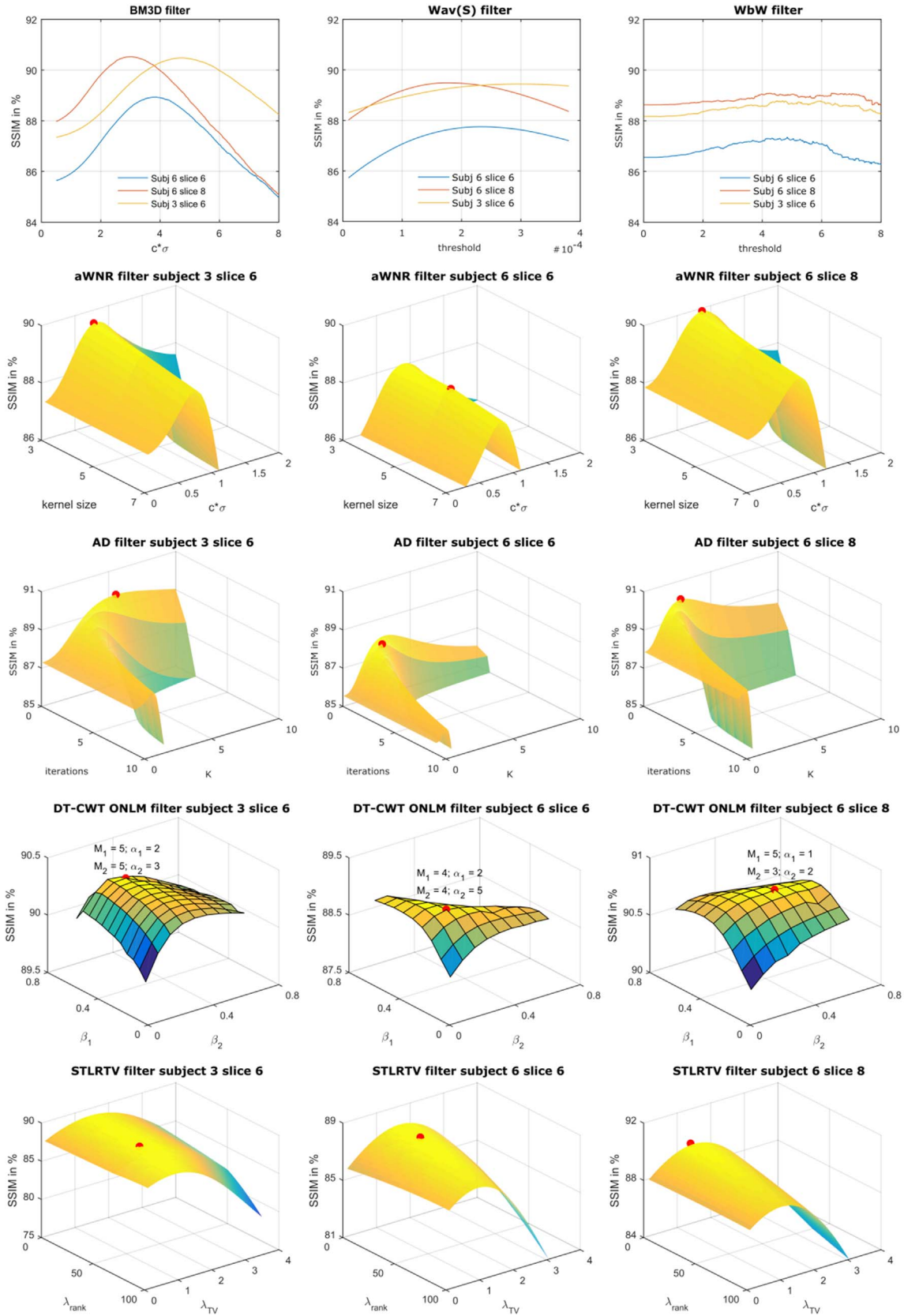
Fig. 3. Results for the reference denoising methods using 3 different slices from the high resolution dataset. In the 3D plots, the maximum is indicated by a red point for a clearer visualization. The optimal parameter for each filtering method varies between different slices of the same subject and also between different subjects.
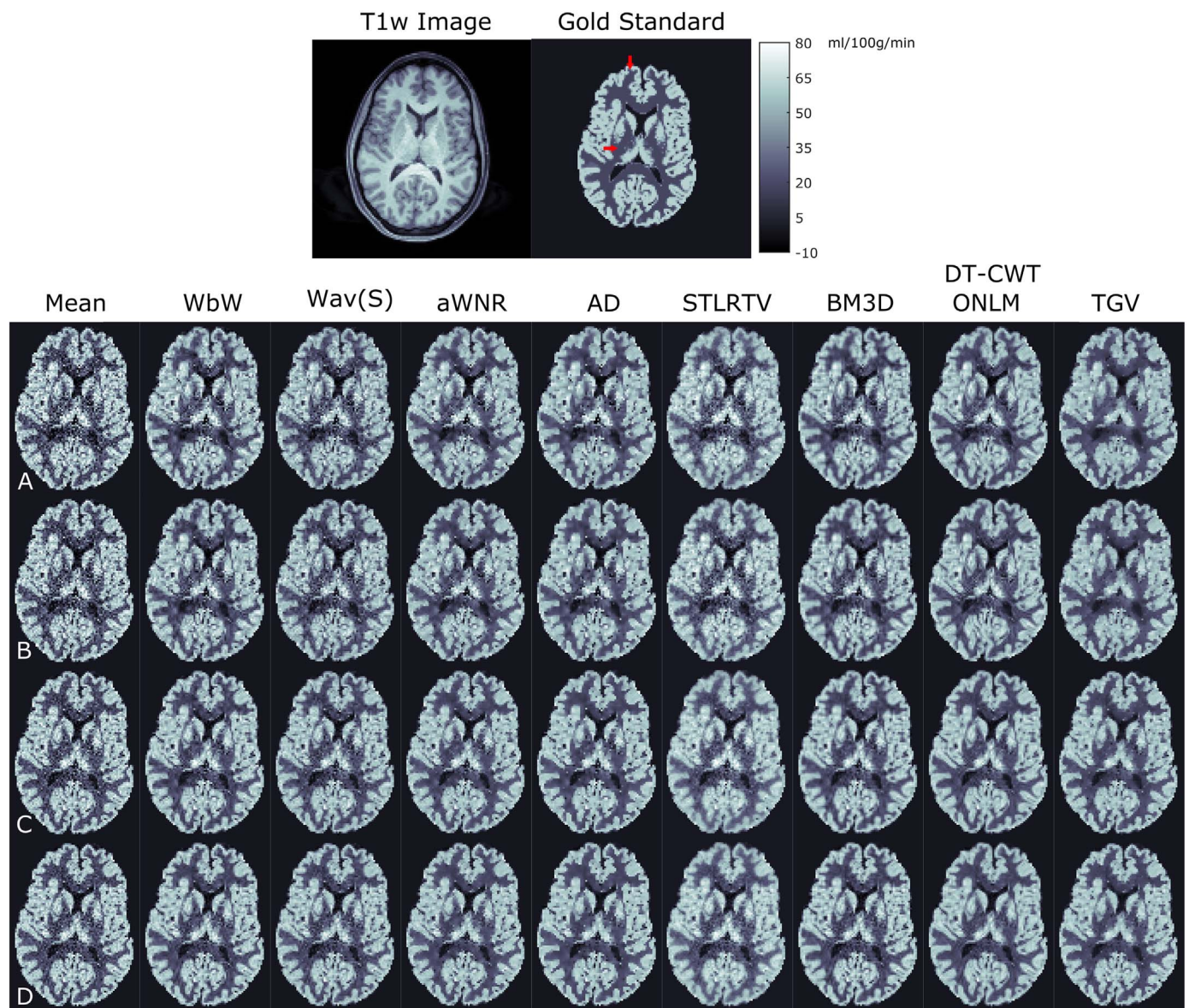
Fig. 4. T1 weighted image, gold standard CBF-map, noisy CBF-map and CBF-map calculated from the denoised difference image using 40 C/L-pairs row A, 50 C/L-pairs row B, 80 C/L-pairs row C and 100 C/L-pairs row D for slice 3 of the synthetic dataset. Areas were the performance of the TGV denoising approach was superior compared to the reference denoising methods are indicated with a red arrow.

PSNR

Peak signal-to-noise ratio (PSNR), PSNR = $20\log_{10}(MAXi/RMSE)$, was used to evaluate the denoising results within the brain mask (Fang et al., 2015; Liang et al., 2015). RMSE denotes the root mean square error between the ground truth CBF-map and the denoised CBF-map and MAXi represent the maximum intensity value in the ground truth CBF-map.

Results

Fig. 3 shows exemplary results of the optimization procedure for each reference denoising method. This figure clearly indicates that the parameters of each reference filter vary between subjects and also

among slices of the same subject. To ensure best possible denoising results of the reference filters, the filter parameters were optimized for each subject and slice. It should be noted, that in contrast to the reference filtering methods our proposed method used the same parameters for all in-vivo datasets listed in Table 1.

Fig. 4 shows exemplary the noise free, the noisy and denoised synthetic CBF maps using 40 (row A), 50 (row B), 80 (row C) and 100 (row D) C/L-pairs. Qualitative comparison of the CBF maps shows a lower level of noise in all denoised CBF maps compared to a simple mean filter. Further, as expected the visual quality of each CBF map increases with increasing number of C/L-pairs. It can be seen that the various denoising techniques result in different noise removal performance and varying degree of spatial smoothing. In comparison to the
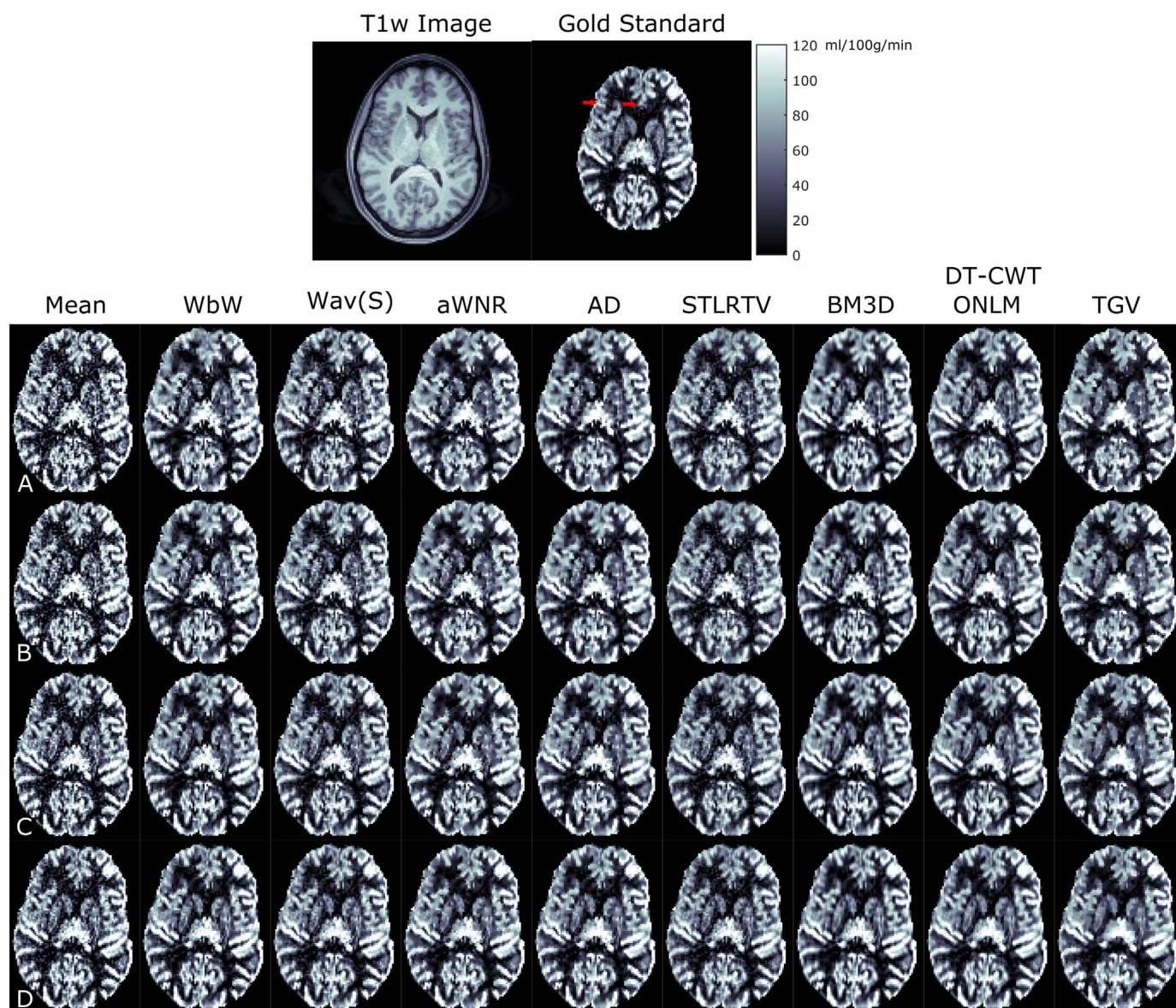
Fig. 5. Top row shows the T1 weighted image and the gold standard CBF-map calculated from 500 C/L-pairs of the high resolution in-vivo dataset of subject 8. Row A to D show the noisy CBF-map and the CBF-map calculated from the denoised difference image using 40 C/L-pairs (row A), 50 C/L-pairs (row B), 80 C/L-pairs (row C) and 100 C/L-pairs (row D). The red arrows indicate areas were the TGV approach is more comparable with the gold standard CBF-map than the CBF-maps from the reference denoising methods.

reference denoising approaches the proposed TGV based method shows improved noise removal, especially in the WM, while small features are still retained. Furthermore, the proposed method shows fewer overestimated CBF values, especially for low SNR (40 and 50 C/L-pairs) datasets.

Fig. 5 shows typical high resolution CBF-maps from subject 8 before and after denoising using 40, 50, 80 and 100 C/L-pairs together with the gold standard CBF-map generated from all 500 C/L-pairs. Similar to the results of the synthetic datasets, the visual quality of the CBF-maps was improved in different ways. Furthermore, the TGV approach removes local outliers in the difference image, which were neither detected by the outlier algorithm nor by one of the seven reference denoising methods, as indicated by a red arrow in Fig. 5.

Such artificial outliers could be misleadingly interpreted as a hyper perfusion showing a clear benefit of the proposed method.

Additionally, Fig. 6 shows a quantitative evaluation of all denoising approaches. The mean SSIM and mean PSNR are given for a different number of C/L-pairs of the high resolution synthetic and in-vivo dataset of subject 8. All denoising results are reported within the generated brain mask. As expected, the PSNR and SSIM increase with increasing numbers of control and label pairs. For low as well as high SNR the proposed approach yields the largest improvement in PSNR and in SSIM. These quantitative results are consistent with the qualitative results in Figs. 4 and 5.

Fig. 7 shows the mean SSIM and mean PSNR for a different number of C/L-pairs of the high resolution synthetic and in-vivo dataset of
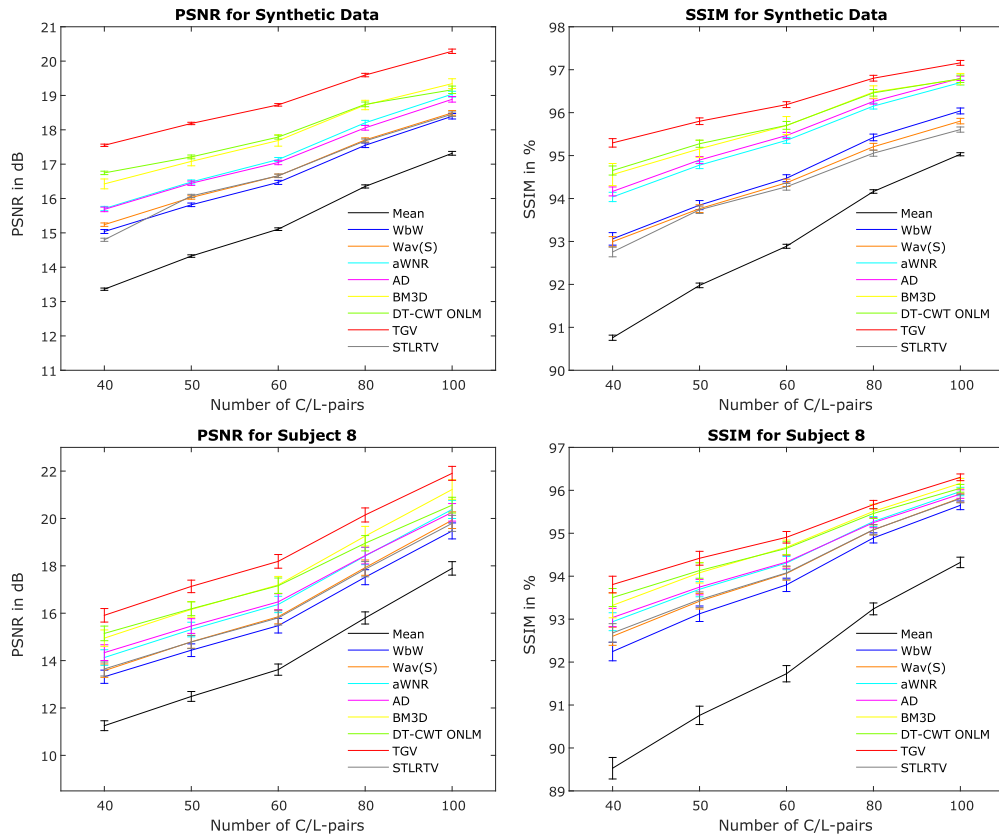
Fig. 6. Mean SSIM and PSNR for different numbers of C/L-pairs from high-resolution in-vivo and synthetic data averaged over 50 trials. Error bars denote ±1 standard deviation.

subject 8. All denoising results are reported within the segmented GM and WM mask.

Fig. 8 shows a representative high resolution CBF-map of each of the remaining seven subjects (subject 1 to subject 7) before and after denoising using 50 C/L-pairs. The filtering results are similar to the denoising results of subject 8.

Fig. 9 shows the mean SSIM and mean PSNR for the high-resolution in-vivo dataset of the remaining 7 subjects using 50 C/L-pairs at optimal filter parameter settings. The TGV approach shows an averaged higher PSNR of 1.1 dB and an averaged higher SSIM of 0.6% compared to the best performing reference denoising technique. It should be noted that for the TGV based approach the same parameters were used for all subjects. The subjects were sorted in ascending order by PSNR.

Fig. 10 shows exemplary the standard resolution CBF-maps before and after denoising from subject 1 for a different number of C/L-pairs. The gold standard CBF-map was calculated from the 100 C/L-pairs. The denoising results for the standard resolution dataset are similar to the results of the high-resolution datasets, with the greatest improvement in visual quality using the proposed TGV based approach.

Fig. 11 shows the mean SSIM and mean PSNR for the two standard-resolution in-vivo datasets for different numbers of C/L-pairs. The SSIM and PSNR improvement for the different filters are in accordance with the results of the high-resolution datasets and the greatest improvement in PSNR and SSIM can be observed for the TGV denoised CBF-maps.

Discussion

The inherently low SNR of ASL data makes spatial denoising essential for robust CBF quantification. The results of this study demonstrate the potential of using a TGV based denoising approach for ASL. Synthetic images and in-vivo images with different SNR levels were considered. Both, synthetic and in-vivo datasets show improved noise suppression for low as well as high SNR regime while retaining small details and edges in the perfusion images. This qualitative improvement is confirmed by the two quantitative metrics SSIM and PSNR. The results of the proposed method were compared with those of seven published denoising approaches. For all denoising methods the filter parameters were optimized with respect to the quantitative metric SSIM, rather than relying on visual quality. This allows comparing the performance of the different filters in a fair way. The utilized parameter optimization strategy might be interesting in general for various denoising algorithms, since it accounts for both structural degradation and differences in contrast. Further, a semi-automatic parameter approach based on the noise variance within an image was implemented (Wells et al., 2010). This approach provides moderate results, but degraded visual quality as well as reduced SSIM and PSNR, compared to the presented optimization approach (data not shown). This is due to the fact that the noise variance is often inaccurately estimated or spatially dependent. In contrast to the reference methods, the TGV filtering approach provides superior results by applying the same model parameter set for all subjects. The optimal model parameters are very robust against varying numbers of averages.
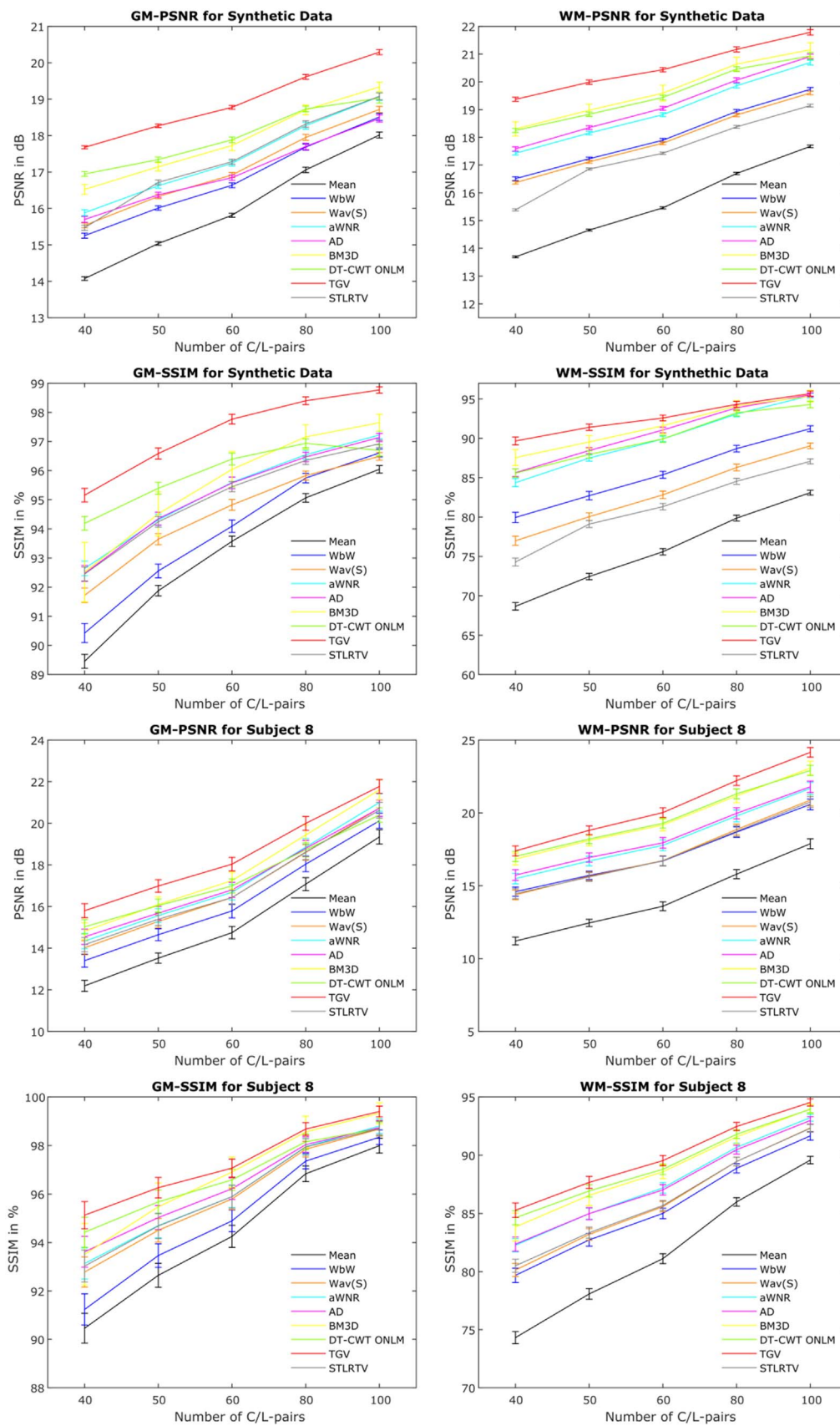
Fig. 7. Mean SSIM and PSNR in the GM and WM for a different number of C/L-pairs from high resolution in-vivo and synthetic data. The results are averaged over 50 trials and the error bars denote ±1 standard deviation.
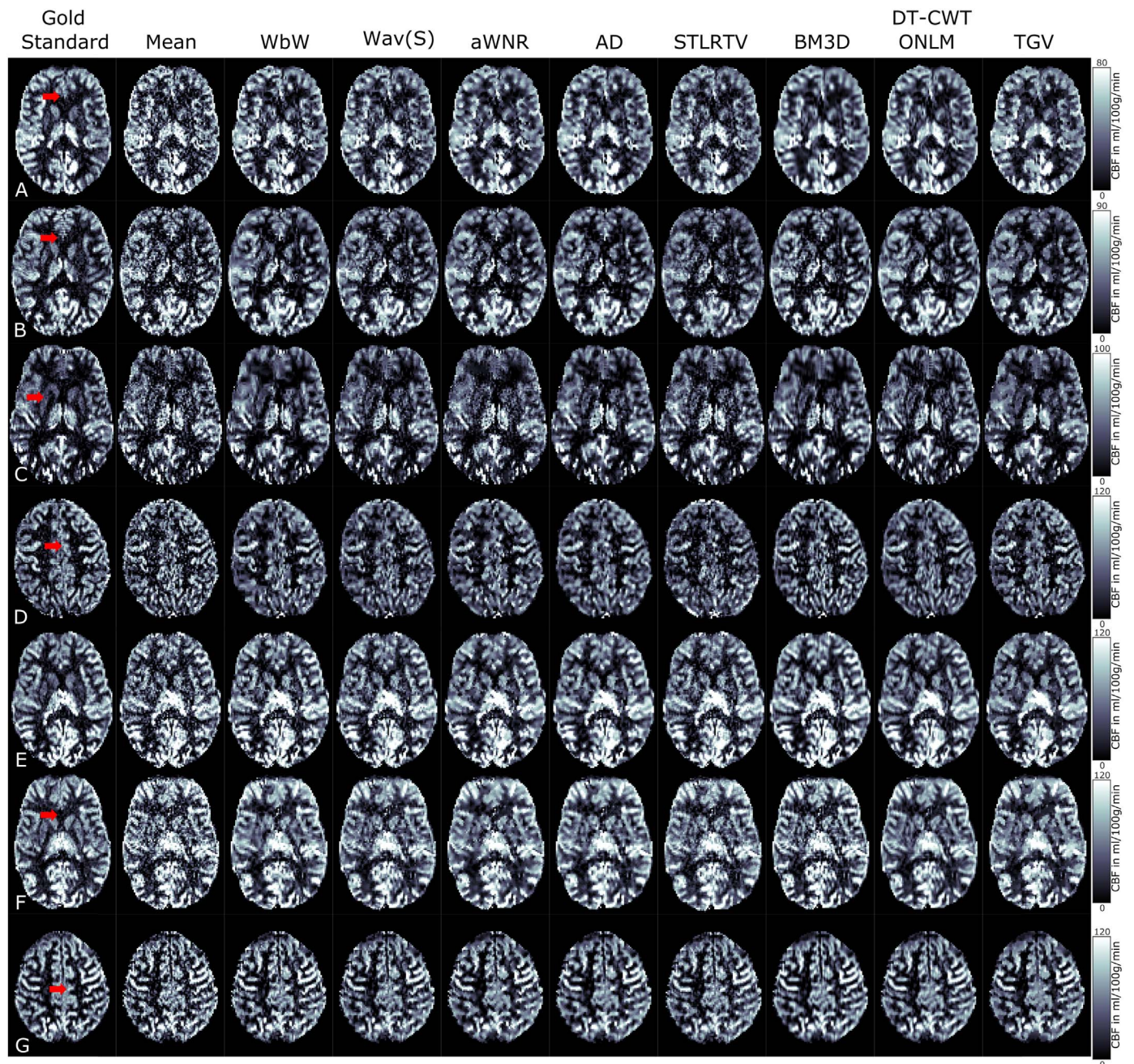
Fig. 8. Gold standard CBF-map, noisy CBF-map and CBF-map calculated from the denoised difference image using 50 C/L-pairs form subject 1–7 (row A to row G). The gold standard CBF-map was calculated from the averaged 500 C/L-pairs. The red arrows indicate areas in the CBF-maps were the TGV approach is more comparable with the gold standard CBF-map than the CBF-maps of the reference denoising methods.

Nevertheless, the regularization parameter λ has to be adapted according to the noise level. In contrast to other methods the proposed method is very robust for a broad range of regularization parameter. Hence, the denoising quality decreases only slightly, especially for datasets with sufficient SNR (Fig. 2). This property might be attributed to the fact that a general denoising model was applied, which does not depend on self-similarity blocks within an image or on a-priori information such as the noise variance, which is often not accurately estimated. This leads also to the fact, that the same parameters can be used for all in-vivo datasets.

In contrast to other studies which added constant zero mean Gaussian noise to the synthetic dataset spatial dependent noise was considered to generate a more realistic synthetic ASL dataset. A comparison of the two Wavelet based filters (WbW and Wav(S)) with the noise free synthetic CBF-map reveals that the structural degradation is minimal. However, noise is still present in the CBF-maps especially in the WM, where the SNR is approximately 3 times smaller than in the GM. The denoising results using AD or aWNR are superior to the two wavelet based filters but in both cases noise is still preserved. This is also the case for the STLRTV denoised CBF-maps. It should be
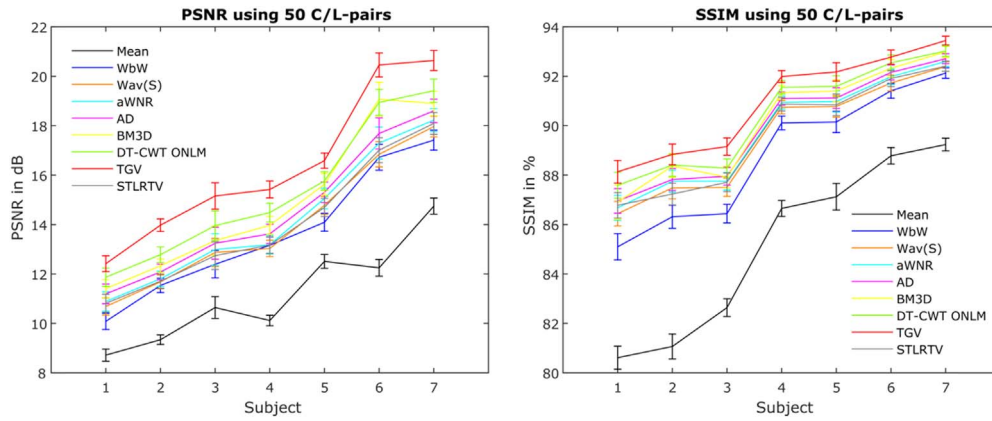
Fig. 9. Mean SSIM and PSNR using 50 C/L-pairs from the remaining 7 subjects averaged over 50 trials. Error bars denote ±1 standard deviation.

noted, that our data is motion-corrected, de-trended and outlier cleared before denoising. This may restrict the benefit of the STLRTV filter compared to non-preprocessed data. For the two block matching filters (BM3D, DT-CW ONLM), based on self-similarity blocks in the difference image, an improved denoising especially in the WM regions can be observed in comparison to the previous filters but this comes at the cost of stronger blurring at the GM/WM boundaries. However, noise is still preserved in the capsula interna for all denoising methods except for the TGV method. The use of self-similarity blocks within a difference image can be a disadvantage in case of blocks or structures which have only a few similar blocks within the image. These blocks remain noisy, which might be the case for the capsula interna (Fig. 4). Further, in all reference-denoised CBF-maps a hyper perfusion can be observed in the left and right thalamus. In contrast, the TGV method resulted in maps which are more comparable to the ground truth. The TGV method shows improved noise removal in the GM and in the WM as well as in the capsula interna. At the same time edges especially in the frontal lobe are still preserved (red arrow in Fig. 4). The retaining of structure and of small details is crucial especially for the application of denoising high resolution ASL data. Furthermore, it is essential for the detection of small local CBF changes which might get vanished in situations where denoising introduces a high degree of spatial smoothing. The oversmoothing of the reference filters may restrict its sensitivity in detecting small changes in CBF. Hence, the reference filters are prone to a limited sensitivity in the detection of small lesions or minor changes in CBF. Furthermore, the inherent spatial oversmoothing of the reference denoising methods could impair the sensitivity in group studies where only GM structures or regions are analyzed.

An increased number of C/L-pairs improve the quality of all CBF-maps and leads to a lower structural degradation, especially for the two block matching filters. This indicates that the degree of spatial smoothing is coupled with the degree of noise suppression and SNR. Moreover, the presented study demonstrates that at low SNR level a trade-off between spatial smoothing and noise removal level has to be chosen for all reference denoising approaches.

These visual observations are confirmed by the two quantitative metrics SSIM and PSNR, indicating a lower systematic error and minor structural degradation for the TGV based method for all analysis. Both, the visual quality and the quantitative metrics show that for all denoising techniques the benefit of denoising decreases with increasing SNR.

The in-vivo dataset exhibits the same degree of spatial oversmoothing for the reference denoising methods (Fig. 5), especially for low SNR. An additional feature of the proposed method is its robustness against outliers. This is achieved by applying the L1 Norm together with the temporal dimension in the data term of the functional (Eq. (4)). This shows a clear benefit of the proposed method, while all reference methods, except the STLRTV, use only the spatial dimension for denoising. In terms of SSIM and PSNR similar results were obtained for the in-vivo datasets of the remaining 7 subjects. The highest improvements are reported for the proposed TGV method. The differences in PSNR and SSIM between subjects may be due to differences in the CBF. Previous studies (Liu et al., 2012; Parkes et al., 2004) found a higher CBF in women than in men. Subjects 1, 2, 3 and 5 are men and subjects 4, 6, 7 and 8 are women indicating a higher PSNR and consequently a higher SSIM for women than men.

Furthermore, we analyzed a PCA and ICA denoising algorithm (Wells et al., 2010) for denoising of the perfusion weighted time series. However, we only use a single TI time with no dynamic change in our data. Denoising by reconstructing the image series using only the biggest components of the PCA clearly reduced the temporal variation of the pixels, but leads, after averaging to the same results as a simple mean filtering of the original data. We observed similar results for the ICA denoised images with no additional improvements. Additionally, it is very hard to choose the right independent components as it is not clear how much each component contributes to the signal. Since we average the whole perfusion weighted time series and got similar results as for simple mean filter, we decided not to include the ICA and PCA results in our study.

We additionally evaluated the denoising algorithm for standard resolution ASL data of two subjects. The performance of the evaluated denoising algorithm (Fig. 10) is the same as for high resolution data with the exception of the STLRTV, which performs better than for the high resolution datasets. This can be due to the higher SNR in the single perfusion weighted images, leading to a higher benefit of the spatial TV and therefore to a better final outcome. However, the proposed TGV based denoising approach is still the best in terms of PSNR and SSIM (Fig. 11).

In summary the results of the presented study highlights, that the proposed TGV method enables an essential reduction of the acquisition time in the application of high as well as standard resolution PASL. As
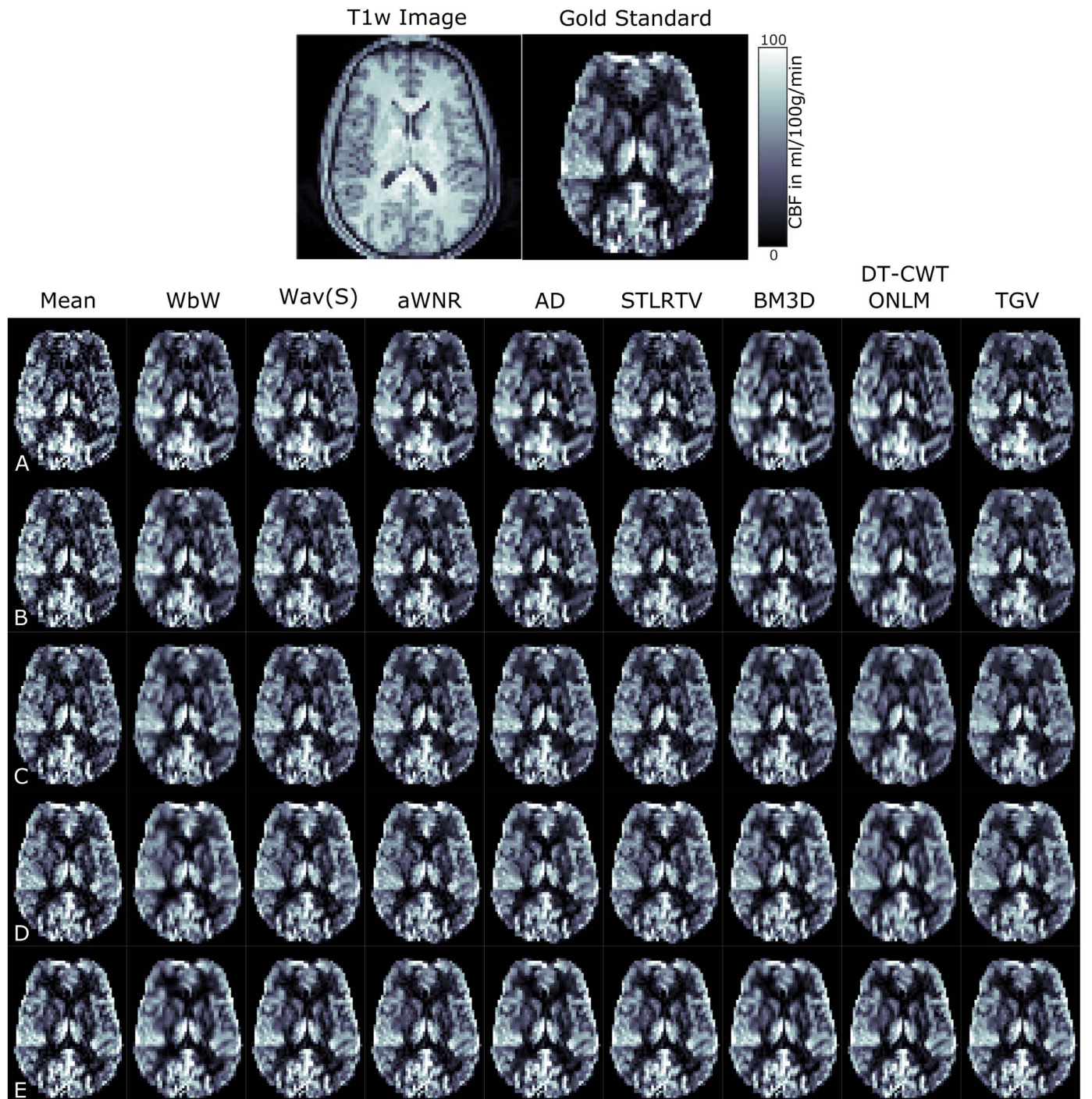
Fig. 10. Top row shows the T1 weighted image and the gold standard CBF-map calculated from 100 C/L-pairs of the standard resolution in-vivo dataset of subject 1. Row A to E show the noisy CBF-map and the CBF-map calculated from the denoised difference image using 8 C/L-pairs (row A), 10 C/L-pairs (row B), 12 C/L-pairs (row C), 15 C/L-pairs (row D) and 20 C/L-pairs (row E).

a consequence, this reduces the risk of motion artifacts and addresses clinical demands. A combination of the proposed TGV denoising method with higher SNR labeling schemes such as pCASL (Dai et al., 2008) or 3D readouts such as 3D-GRASE (Günther et al., 2005) would lead to a further reduction in acquisition time or may further improve the spatial resolution. The developed algorithm can be easily implemented as an additional pre-processing step besides motion-correction, outlier-detection and temporal filtering and should help increasing the robustness and reproducibility of CBF quantification in clinical studies.
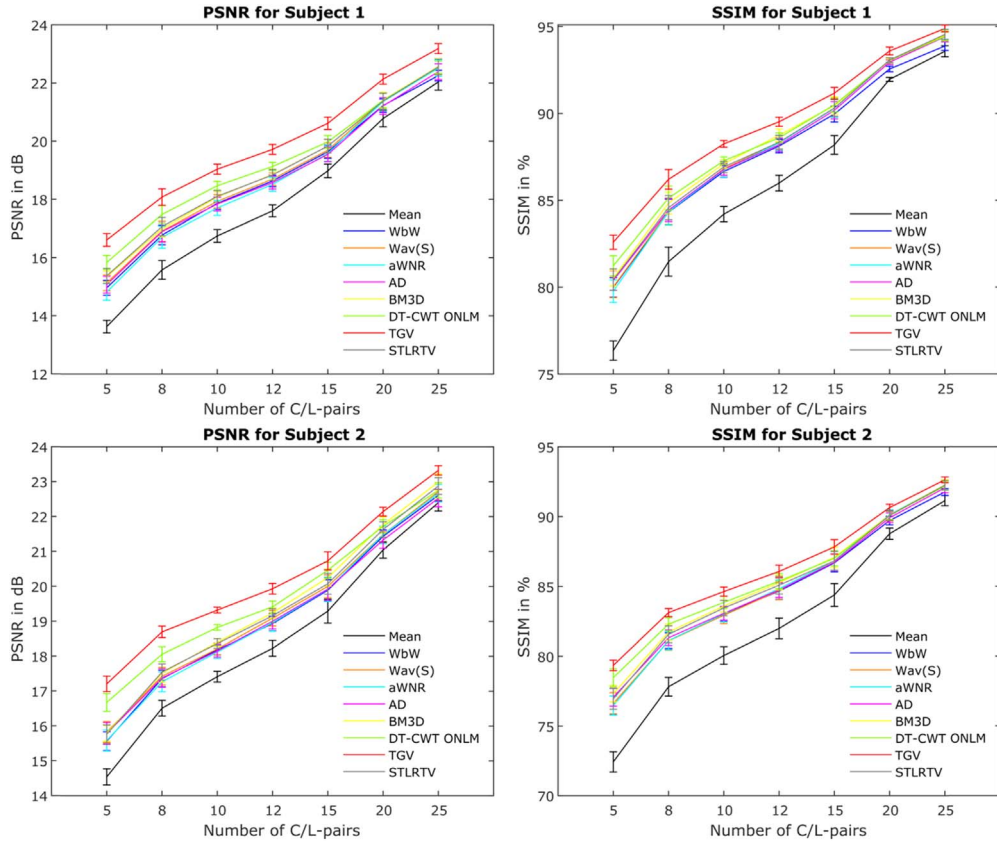
Fig. 11. Mean SSIM and PSNR for different numbers of C/L-pairs from the two standard-resolution in-vivo datasets averaged over 50 trials. Error bars denote ±1 standard deviation.

Conclusion

This study demonstrated that the proposed total generalized variation denoising framework with coupling of control and label pairs, outperforms state of the art denoising techniques. In addition, the new method improved the quantification accuracy of the CBF-maps, for both simulations and experiments. This general TGV model joins spatial and temporal similarity of the label and difference image for robust signal estimation, in case of low as well as high SNR. Consequently, this approach highly satisfies clinical demands in terms of reducing the scan time, motion artifacts and local outliers and

increasing the spatial resolution. Compared to other state of the art denoising methods the structural degradation is minimized and local outliers are removed. This makes the TGV denoising approach highly attractive in group or functional ASL studies as well as for detecting anomalies in perfusion.

Acknowledgements

Appendix

The problem defined in *Denoising setup* is reformulated as a saddle-point problem. Therefore the norms in the problem are dualized, cf. (Bredies, 2014), which introduces additional "dual" variables P, Q, p, q, r, s. Let w be the additional variable necessary to define the TGV functional of the $u_c - u_l$ term, i.e. this variable corresponds to v in the definition of the TGV terms for u_l. Setting $x = (u_c, u_l, w, v)$ and $y = (P, Q, p, r, q, s)$ yields

$$\mathcal{K} = \begin{pmatrix} \mathcal{S} & 0 & 0 & 0 \\ 0 & \mathcal{S} & 0 & 0 \\ 0 & \nabla & 0 & -\mathrm{Id} \\ \nabla & -\nabla & -\mathrm{Id} & 0 \\ 0 & 0 & 0 & \mathcal{E} \\ 0 & 0 & \mathcal{E} & 0 \end{pmatrix}$$

$$\mathcal{F}(x) = 0$$

$$\mathcal{G}(y) = \langle u_c^d | P \rangle + I_\lambda(P) + \langle u_l^d | Q \rangle + I_\lambda(Q) + I_{\gamma_1 \alpha_1}(p) + I_{\gamma_1 \alpha_0}(q) + I_{\gamma_2 \alpha_1}(r) + I_{\gamma_2 \alpha_0}(s),$$

as the saddle-point functions. In the above formulas $I_a(b)$ is the indicator function of the $\|\cdot\|_\infty$ ball of size a evaluated at point b, i.e. it is zero if $\|b\|_\infty \leq a$, and ∞ otherwise.

Iterative scheme

With the above notation the aforementioned algorithm of Chambolle and Pock (2011) can be written as

$$y^{n+1} = (I + \sigma \partial G)^{-1}(y^n + \sigma K \bar{x}^n)$$
$$x^{n+1} = (I + \tau \partial F^*)^{-1}(x^n - \tau K^* y^{n+1})$$
$$\bar{x}^{n+1} = 2x^{n+1} - x^n,$$

where ∂G is the subgradient of G and ∂F^* denotes the subgradient of the Fenchel conjugate F^*, cf. (Schuster et al., 2012), and the positive step-sizes σ and τ are such that $\sigma\tau\|K\|^2 < 1$. In our case a series of elementary, but tedious, calculations leads to the iteration scheme:

$$P^{n+1} = P_\lambda(P^n + \sigma(\mathcal{S}\bar{u}_c^n - u_c^\delta))$$
$$Q^{n+1} = P_\lambda(Q^n + \sigma(\mathcal{S}\bar{u}_l^n - u_l^\delta))$$
$$p^{n+1} = P_{\gamma_1\alpha_1}(p^n + \sigma(\nabla\bar{u}_l^n - \bar{v}^n))$$
$$r^{n+1} = P_{\gamma_2\alpha_1}(r^n + \sigma(\nabla(\bar{u}_c^n - \bar{u}_l^n) - \bar{w}^n))$$
$$q^{n+1} = P_{\gamma_1\alpha_0}(q^n + \sigma\mathcal{E}\bar{v}^n)$$
$$s^{n+1} = P_{\gamma_2\alpha_0}(s^n + \sigma\mathcal{E}\bar{w}^n)$$
$$u_c^{n+1} = u_c^n + \tau(\mathrm{div}\, r^{n+1} - \mathcal{S}^*P^{n+1})$$
$$u_l^{n+1} = u_l^n + \tau(\mathrm{div}(p^{n+1} - r^{n+1}) - \mathcal{S}^*Q^{n+1})$$
$$v^{n+1} = v^n + \tau(p^{n+1} + \mathrm{div}\, q^{n+1})$$
$$w^{n+1} = w^n + \tau(r^{n+1} + \mathrm{div}\, s^{n+1})$$
$$\bar{u}_c^{n+1} = 2u_c^{n+1} - u_c^n$$
$$\bar{u}_l^{n+1} = 2u_l^{n+1} - u_l^n$$
$$\bar{v}^{n+1} = 2v^{n+1} - v^n$$
$$\bar{w}^{n+1} = 2w^{n+1} - w^n$$

In the above formulas $P_a(b)_{i,j,k} = b_{i,j,k}/\max\{1, \|b_{i,j,:}\|_2/a\}$ and the divergence operators are chosen such that they are adjoint to the gradient and symmetrized gradient respectively. Details on the implementation of such divergences can be found in Bredies (2014).

References

Addicott, M.A., Yang, L.L., Peiffer, A.M., Burnett, L.R., Burdette, J.H., Chen, M.Y., Hayasaka, S., Kraft, R.A., Maldjian, J.A., Laurienti, P.J., 2009. The effect of daily caffeine use on cerebral blood flow: how much caffeine can we tolerate? Hum. Brain Mapp. 30, 3102–3114. http://dx.doi.org/10.1002/hbm.20732.

Alsop, D.C., Detre, J.A., Golay, X., Günther, M., Hendrikse, J., Hernandez-Garcia, L., Lu, H., MacIntosh, B.J., Parkes, L.M., Smits, M., van Osch, M.J.P., Wang, D.J.J., Wong, E.C., Zaharchuk, G., 2015. Recommended implementation of arterial spin-labeled perfusion MRI for clinical applications: a consensus of the ISMRM perfusion study group and the European consortium for ASL in dementia. Magn. Reson. Med. 73, 102–116. http://dx.doi.org/10.1002/mrm.25607.

Asllani, I., Borogovac, A., Brown, T.R., 2008. Regression algorithm correcting for partial volume effects in arterial spin labeling MRI. Magn. Reson. Med. 60, 1362–1371. http://dx.doi.org/10.1002/mrm.21670.

Asllani, I., Habeck, C., Borogovac, A., Brown, T.R., Brickman, A.M., Stern, Y., 2009. Separating function from structure in perfusion imaging of the aging brain. Hum. Brain Mapp. 30, 2927–2935. http://dx.doi.org/10.1002/hbm.20719.

Bammer, R. (Roland), 2016. MR and CT Perfusion Imaging: Clinical Applications and Theoretical Principles. Wolters Kluwer, Philadelphia.

Bause, J., Ehses, P., Mirkes, C., Shajan, G., Scheffler, K., Pohmann, R., 2016. Quantitative and functional pulsed arterial spin labeling in the human brain at 9.4 T. Magn. Reson. Med. 75, 1054–1063. http://dx.doi.org/10.1002/mrm.25671.

Behzadi, Y., Restom, K., Liau, J., Liu, T.T., 2007. A component based noise correction method (CompCor) for BOLD and perfusion based fMRI. Neuroimage 37, 90–101. http://dx.doi.org/10.1016/j.neuroimage.2007.04.042.

Bibic, A., Knutsson, L., Ståhlberg, F., Wirestam, R., 2010. Denoising of arterial spin labeling data: wavelet-domain filtering compared with Gaussian smoothing. MAGMA 23, 125–137. http://dx.doi.org/10.1007/s10334-010-0209-8.

Borogovac, A., Habeck, C., Small, S.A., Asllani, I., 2010. Mapping brain function using a 30-day interval between baseline and activation: a novel arterial spin labeling fMRI approach. J. Cereb. Blood Flow Metab. 30, 1721–1733. http://dx.doi.org/10.1038/jcbfm.2010.89.

Bredies, K., 2014. Recovering piecewise smooth multichannel images by minimization of convex functionals with total generalized variation penalty. in: Lecture Notes in Computer Science (Including Subseries Lecture Notes in Artificial Intelligence and Lecture Notes in Bioinformatics). Springer Berlin Heidelberg, pp. 44–77. http://dx.doi.org/10.1007/978-3-642-54774-4_3.

Bredies, K., Holler, M., 2015. A TGV-based framework for variational image decompression, zooming, and reconstruction. Part I: analytics. SIAM J. Imaging Sci. 8, 2814–2850. http://dx.doi.org/10.1137/15M1023865.

Bredies, K., Kunisch, K., Pock, T., 2010. Total generalized variation. SIAM J. Imaging Sci.

3, 492–526. http://dx.doi.org/10.1137/090769521.

Bredies, K., Valkonen, T., 2011. Inverse problems with second-order total generalized variation constraints. Int. Conf. Sampl. Theory Appl., 1–4.

Buxton, R.B., Frank, L.R., Wong, E.C., Siewert, B., Warach, S., Edelman, R.R., 1998. A general kinetic model for quantitative perfusion imaging with arterial spin labeling. Magn. Reson. Med. 40, 383–396. http://dx.doi.org/10.1002/mrm.1910400308.

Chambolle, A., Pock, T., 2011. A first-order primal-dual algorithm for convex problems with applications to imaging. J. Math. Imaging Vis. 40, 120–145. http://dx.doi.org/10.1007/s10851-010-0251-1.

Dabov, K., Foi, A., Katkovnik, V., Egiazarian, K., 2007. Image denoising by sparse 3-D transform-domain collaborative filtering. IEEE Trans. Image Process. 16, 2080–2095. http://dx.doi.org/10.1109/TIP.2007.901238.

Dai, W., Garcia, D., de Bazelaire, C., Alsop, D.C., 2008. Continuous flow-driven inversion for arterial spin labeling using pulsed radio frequency and gradient fields. Magn. Reson. Med. 60, 1488–1497. http://dx.doi.org/10.1002/mrm.21790.

Daubechies, I., Defrise, M., De Mol, C., 2004. An iterative thresholding algorithm for linear inverse problems with a sparsity constraint. Commun. Pure Appl. Math. 57, 1413–1457. http://dx.doi.org/10.1002/cpa.20042.

Detre, J.A., Leigh, J.S., Williams, D.S., Koretsky, A.P., 1992. Perfusion imaging. Magn. Reson. Med. 23, 37–45. http://dx.doi.org/10.1002/mrm.1910230106.

Dobson, D.C., Santosa, F., 1996. Recovery of blocky images from noisy and blurred data. SIAM J. Appl. Math. 56, 1181–1198. http://dx.doi.org/10.1137/S003613999427560X.

Domino, E.F., Ni, L., Xu, Y., Koeppe, R.A., Guthrie, S., Zubieta, J.-K., 2004. Regional cerebral blood flow and plasma nicotine after smoking tobacco cigarettes. Prog. Neuropsychopharmacol. Biol. Psychiatry 28, 319–327. http://dx.doi.org/10.1016/j.pnpbp.2003.10.011.

Fang, R., Huang, J., Luh, W.-M., 2015. A spatio-temporal low-rank total variation approach for denoising arterial spin labeling MRI data. In: Proceedings of the 2015 IEEE 12th International Symposium on Biomedical Imaging (ISBI). IEEE. pp. 498–502. http://dx.doi.org/10.1109/ISBI.2015.7163920.

Fazlollahi, A., Bourgeat, P., Liang, X., Meriaudeau, F., Connelly, A., Salvado, O., Calamante, F., 2015. Reproducibility of multiphase pseudo-continuous arterial spin labeling and the effect of post-processing analysis methods. Neuroimage 117, 191–201. http://dx.doi.org/10.1016/j.neuroimage.2015.05.048.

Gardener, A.G., Gowland, P.A., Francis, S.T., 2009. Implementation of quantitative perfusion imaging using pulsed arterial spin labeling at ultra-high field. Magn. Reson. Med. 61, 874–882. http://dx.doi.org/10.1002/mrm.21796.

Günther, M., Oshio, K., Feinberg, D.A., 2005. Single-shot 3D imaging techniques improve arterial spin labeling perfusion measurements. Magn. Reson. Med. 54, 491–498. http://dx.doi.org/10.1002/mrm.20580.

Herscovitch, P., Raichle, M.E., 1985. What is the correct value for the brain–blood partition coefficient for water? J. Cereb. Blood Flow Metab. 5, 65–69. http://

dx.doi.org/10.1038/jcbfm.1985.9.

Knoll, F., Bredies, K., Pock, T., Stollberger, R., 2011. Second order total generalized variation (TGV) for MRI. Magn. Reson. Med. 65, 480–491. http://dx.doi.org/10.1002/mrm.22595.

Le Gall, D., Tabatabai, A., 1988. Sub-band coding of digital images using symmetric short kernel filters and arithmetic coding techniques. In: Proceedings of the International Conference on Acoustics, Speech, and Signal Processing (ICASSP-88). IEEE. Vol.2. pp. 761–764. http://dx.doi.org/10.1109/ICASSP.1988.196696.

Leenders, K.L., Perani, D., Lammertsma, A.A., Heather, J.D., Buckingham, P., Healy, M.J., Gibbs, J.M., Wise, R.J., Hatazawa, J., Herold, S., 1990. Cerebral blood flow, blood volume and oxygen utilization. Normal values and effect of age. Brain, 27–47.

Liang, X., Connelly, A., Calamante, F., 2013. Improved partial volume correction for single inversion time arterial spin labeling data. Magn. Reson. Med. 69, 531–537. http://dx.doi.org/10.1002/mrm.24279.

Liang, X., Connelly, A., Calamante, F., 2015. Voxel-wise functional connectomics using arterial spin labeling functional magnetic resonance imaging: the role of denoising. Brain Connect. 5, 543–553. http://dx.doi.org/10.1089/brain.2014.0290.

Liu, Y., Zhu, X., Feinberg, D., Guenther, M., Gregori, J., Weiner, M.W., Schuff, N., 2012. Arterial spin labeling MRI study of age and gender effects on brain perfusion hemodynamics. Magn. Reson. Med. 68, 912–922. http://dx.doi.org/10.1002/mrm.23286.

Lu, H., Clingman, C., Golay, X., van Zijl, P.C.M., 2004. Determining the longitudinal relaxation time (T1) of blood at 3.0 T. Magn. Reson. Med. 52, 679–682. http://dx.doi.org/10.1002/mrm.20178.

Luh, W.M., Wong, E.C., Bandettini, P.A., Hyde, J.S., 1999. QUIPSS II with thin-slice TI1 periodic saturation: a method for improving accuracy of quantitative perfusion imaging using pulsed arterial spin labeling. Magn. Reson. Med. 41, 1246–1254.

Maumet, C., Maurel, P., Ferré, J.-C., Barillot, C., 2014. Robust estimation of the cerebral blood flow in arterial spin labelling. Magn. Reson. Imaging 32, 497–504. http://dx.doi.org/10.1016/j.mri.2014.01.016.

Parkes, L.M., Rashid, W., Chard, D.T., Tofts, P.S., 2004. Normal cerebral perfusion measurements using arterial spin labeling: reproducibility, stability, and age and gender effects. Magn. Reson. Med. 51, 736–743. http://dx.doi.org/10.1002/mrm.20023.

Petr, J., Ferre, J.-C., Gauvrit, J.-Y., Barillot, C., 2010a. Denoising arterial spin labeling MRI using tissue partialvolume. In: Proceedings of the SPIE Medical Imaging 2010: Image Pro-cessing, San Diego. pp. 76230L. http://dx.doi.org/10.1117/12.844443.

Petr, J., Ferre, J.-C., Gauvrit, J.-Y., Barillot, C., 2010b. Improving arterial spin labeling data by temporal filtering. In: Proceedings of the SPIE Medical Imaging 2010: Image Pro-cessing, San Diego. pp. 76233B. http://dx.doi.org/10.1117/12.843960.

Pfeuffer, J., Adriany, G., Shmuel, A., Yacoub, E., Van De Moortele, P.-F., Hu, X., Ugurbil, K., 2002. Perfusion-based high-resolution functional imaging in the human brain at 7 T. Magn. Reson. Med. 47, 903–911. http://dx.doi.org/10.1002/mrm.10154.

Pöschl, C., Scherzer, O., 2015. Exact solutions of one-dimensional total generalized variation. Commun. Math. Sci. 13, 171–202. http://dx.doi.org/10.4310/CMS.2015.v13.n1.a9.

Raoult, H., Petr, J., Bannier, E., Stamm, A., Gauvrit, J.-Y., Barillot, C., Ferré, J.-C., 2011. Arterial spin labeling for motor activation mapping at 3 T with a 32-channel coil: reproducibility and spatial accuracy in comparison with BOLD fMRI. Neuroimage 58, 157–167. http://dx.doi.org/10.1016/j.neuroimage.2011.06.011.

Rudin, L.I., Osher, S., Fatemi, E., 1992. Nonlinear total variation based noise removal algorithms. Phys. D Nonlinear Phenom. 60, 259–268. http://dx.doi.org/10.1016/0167-2789(92)90242-F.

Schloegl, M., Holler, M., Schwarzl, A., Bredies, K., Stollberger, R., 2016. Infimal convolution of total generalized variation functionals for dynamic MRI. Magn. Reson. Med.. http://dx.doi.org/10.1002/mrm.26352.

Schuster, T., Kaltenbacher, B., Hofmann, B., Kazimierski, K.S., 2012. Regularization Methods in Banach Spaces. Walter de Gruyter, Berlin.

Shirzadi, Z., Crane, D.E., Robertson, A.D., Maralani, P.J., Aviv, R.I., Chappell, M.A.,

Goldstein, B.I., Black, S.E., MacIntosh, B.J., 2015. Automated removal of spurious intermediate cerebral blood flow volumes improves image quality among older patients: a clinical arterial spin labeling investigation. J. Magn. Reson. Imaging 42, 1377–1385. http://dx.doi.org/10.1002/jmri.24918.

Tan, H., Maldjian, J.A., Pollock, J.M., Burdette, J.H., Yang, L.Y., Deibler, A.R., Kraft, R.A., 2009. A fast, effective filtering method for improving clinical pulsed arterial spin labeling MRI. J. Magn. Reson. Imaging 29, 1134–1139. http://dx.doi.org/10.1002/jmri.21721.

Teeuwisse, W.M., Webb, A.G., van Osch, M.J.P., 2010. Arterial spin labeling at ultra-high field: all that glitters is not gold. Int. J. Imaging Syst. Technol. 20, 62–70. http://dx.doi.org/10.1002/ima.20218.

van Gelderen, P., de Zwart, J.A., Duyn, J.H., 2008. Pittfalls of MRI measurement of white matter perfusion based on arterial spin labeling. Magn. Reson. Med. 59, 788–795. http://dx.doi.org/10.1002/mrm.21515.

Vidorreta, M., Wang, Z., Rodríguez, I., Pastor, M.A., Detre, J.A., Fernández-Seara, M.A., 2013. Comparison of 2D and 3D single-shot ASL perfusion fMRI sequences. Neuroimage 66, 662–671. http://dx.doi.org/10.1016/j.neuroimage.2012.10.087.

Vidyasagar, R., Greyling, A., Draijer, R., Corfield, D.R., Parkes, L.M., 2013. The effect of black tea and caffeine on regional cerebral blood flow measured with arterial spin labeling. J. Cereb. Blood Flow Metab. 33, 963–968. http://dx.doi.org/10.1038/jcbfm.2013.40.

Wang, J., Alsop, D.C., Li, L., Listerud, J., Gonzalez-At, J.B., Schnall, M.D., Detre, J.A., 2002. Comparison of quantitative perfusion imaging using arterial spin labeling at 1.5 and 4.0 T. Magn. Reson. Med. 48, 242–254. http://dx.doi.org/10.1002/mrm.10211.

Wang, Z., 2012. Improving cerebral blood flow quantification for arterial spin labeled perfusion MRI by removing residual motion artifacts and global signal fluctuations. Magn. Reson. Imaging 30, 1409–1415. http://dx.doi.org/10.1016/j.mri.2012.05.004.

Wang, Z., Aguirre, G.K., Rao, H., Wang, J., Fernández-Seara, M.A., Childress, A.R., Detre, J.A., 2008. Empirical optimization of ASL data analysis using an ASL data processing toolbox: ASLtbx. Magn. Reson. Imaging 26, 261–269. http://dx.doi.org/10.1016/j.mri.2007.07.003.

Wang, Z., Bovik, A.C., Sheikh, H.R., Simoncelli, E.P., 2004. Image quality assessment: from error visibility to structural similarity. IEEE Trans. Image Process. 13, 600–612. http://dx.doi.org/10.1109/TIP.2003.819861.

Wang, Z., Das, S.R., Xie, S.X., Arnold, S.E., Detre, J.A., Wolk, D.A., 2013. Arterial spin labeled MRI in prodromal Alzheimer's disease: a multi-site study. NeuroImage Clin. 2, 630–636. http://dx.doi.org/10.1016/j.nicl.2013.04.014.

Wells, J.A., Thomas, D.L., King, M.D., Connelly, A., Lythgoe, M.F., Calamante, F., 2010. Reduction of errors in ASL cerebral perfusion and arterial transit time maps using image de-noising. Magn. Reson. Med. 64, 715–724. http://dx.doi.org/10.1002/mrm.22319.

Wong, E.C., Buxton, R.B., Frank, L.R., 1997. Implementation of quantitative perfusion imaging techniques for functional brain mapping using pulsed arterial spin labeling. NMR Biomed. 10, 237–249.

Wong, E.C., Buxton, R.B., Frank, L.R., 1998. A theoretical and experimental comparison of continuous and pulsed arterial spin labeling techniques for quantitative perfusion imaging. Magn. Reson. Med. 40, 348–355.

Zhang, J., 2016. How far is arterial spin labeling MRI from a clinical reality? Insights from arterial spin labeling comparative studies in Alzheimer's disease and other neurological disorders. J. Magn. Reson. Imaging 43, 1020–1045. http://dx.doi.org/10.1002/jmri.25022.

Zhang, K., Herzog, H., Mauler, J., Filss, C., Okell, T.W., Kops, E.R., Tellmann, L., Fischer, T., Brocke, B., Sturm, W., Coenen, H.H., Shah, N.J., 2014. Comparison of cerebral blood flow acquired by simultaneous [15O] water positron emission tomography and arterial spin labeling magnetic resonance imaging. J. Cereb. Blood Flow Metab. 34, 1373–1380. http://dx.doi.org/10.1038/jcbfm.2014.92.